

# Geo-neutrinos as indicators of the origin and thermal history of the Earth

S.T. Dye

College of Natural Sciences, Hawaii Pacific University, Kaneohe, HI, 96744 USA

Department of Physics and Astronomy, University of Hawaii, Honolulu, HI, 96822 USA

## **Abstract**

Geological models are at odds over the radioactive power of the earth, predicting anywhere from 16 to 42 TW. The actual value constrains the thermal evolution and indicates the meteoritic origin of the planet. An estimated 20% of this radioactive power escapes to space in the form of geo-neutrinos. The remaining portion heats the planet with significant geo-dynamical consequences. The amount of radiogenic heating, conveniently expressed as a fraction of the 47-TW surface heat flow, discriminates earth models and characterizes the rate of planetary temperature change. A fraction greater than one means the earth is heating up; a fraction less than one means the earth is cooling down. Radiogenic heating in the planet primarily springs from unstable nuclides of uranium, thorium, and potassium. Closely associated with radiogenic heating is the production of geo-neutrinos. Large sub-surface detectors efficiently record the infrequent interactions of the highest energy geo-neutrinos, which originate from uranium and thorium. The measured energy spectrum of the interactions estimates the relative amounts of these heat-producing elements, while the intensity assesses planetary radiogenic power. Recent geo-neutrino observations suggest radioactivity accounts for less than all of the surface heat flow. This assessment, implying the earth is cooling down, approaches sensitivity to model predictions. Future observations at selected locations have the potential to constrain the thermal evolution of the planet and to resolve earth models. This Letter reviews the science and status of geo-neutrino observations and the prospects for measuring the radioactive power of the planet.

*Keywords:* geo-neutrino; terrestrial heat.

PACS Nos.: 91.35.-x; 13.15.+g; 14.60.Pq; 23.40.Bw ; 91.67.fm.

## **1. Introduction**

Heat flows from the surface of the earth at a measured rate of  $47 \pm 2$  TW (Davies and Davies, 2010). An unknown portion of the surface heat flow derives from the decay of radioactive elements. Conservation of energy suggests that terrestrial temperature change depends on the difference between internal heating and surface heat flow. The magnitude of radiogenic heating constrains the thermal evolution of the planet.

Chemical models of the earth have close associations with two groups of chondritic meteorites. These groups, which are considered representative of the solar nebula from which earth accreted, have similar abundances of heat-producing elements (Wasson

and Kallemeyn, 1988). Enstatite chondrites (EH) have stable isotope compositions and iron content comparable to terrestrial values. This motivates the enstatite earth model (Javoy et al., 2010). Low abundances of volatile elements in this meteorite group limit radiogenic heating in an enstatite earth to 11-14 TW. Carbonaceous chondrites (CI) have nonvolatile element composition similar to the solar photosphere (Palme and Jones, 2003). These meteorites are rich in volatile elements (Wasson and Kallemeyn, 1988). Assuming ~40% of the accreting mass is lost due to non-condensation builds a carbonaceous earth with 17-19 TW of radiogenic heating (Rocholl and Jochum, 1993). These EH and CI earth models predict distinctly different amounts of terrestrial radiogenic heating. The magnitude of radiogenic heating constrains the meteoritic origin of the planet.

Geophysical models (GP) describe terrestrial heat transfer through thermal convection of the mantle. Achieving viable viscosity requires more mantle heating than afforded by geochemical models. Two physical earth models define a representative range of terrestrial radiogenic heating, predicting 27-35 TW (Turcotte et al., 2001). Geophysical earth models predict significantly higher levels of radiogenic heating than geochemical models.

Comparing the chemical and physics earth models by the ratio of the predicted radiogenic heating to the surface heat flow puts the EH model at 0.24-0.30, the CI model at 0.37-0.42, and the GP model at 0.57-0.73. These geological models predict that the earth is cooling down at different rates. The magnitude of terrestrial radiogenic heating discriminates these models. Although there are clear differences in the model ratios, there presently exist no experimental assessments of terrestrial radiogenic heating that resolve these predictions.

Terrestrial radiogenic heating primarily derives from nuclides of uranium, thorium, and potassium (Van Schmus, 1995). These elements condense as oxides, giving them chemical affinity for the silicate crust and mantle. Typical terrestrial ratios of these elements ( $\text{Th}/\text{U}\approx 4$  and  $\text{K}/\text{U}\approx 10^4$ ) project dominant contributions to radiogenic heating from uranium and thorium, with potassium supplying the bulk of the remainder (Arevalo et al., 2009).

Intimately related to terrestrial radiogenic heating is the flux of geo-neutrinos (Fiorentini et al., 2007). Beta decays of daughter nuclides in the radioactive series of  $^{238}\text{U}$  and  $^{232}\text{Th}$  produce detectable geo-neutrinos. Geo-neutrinos are currently being observed underground in Japan (Araki et al., 2005b) and Italy (Bellini et al., 2010). These observations, estimating both the number and the energy spectrum of geo-neutrino interactions, together with several assumptions about the global distribution of uranium and thorium, suggest planetary radiogenic heating smaller than the surface heat flow (Gando et al., 2011). This sensitivity, approaching a level of geological interest, prompts an assessment of the capability of future observations with dedicated detection projects.

The global distribution of radiogenic heating significantly influences the surface geo-neutrino flux as well as the structure, dynamic activity, and thermal history of the planet (Jaupart et al., 2007; Korenaga, 2008; Lay et al., 2008, Mareschal et al., 2011). There are three seismically distinct earth layers: crust, mantle, and core. The chemical affinity of uranium, thorium, and potassium suggest insignificant amounts of radiogenic heating and geo-neutrino production in the metallic core (McDonough, 2003). Radiogenic heating in the crust is relatively robustly estimated at  $8 \pm 1$  TW (Rudnick and Gao, 2003). The difference between the planetary heating predicted by the various earth models and the estimated crust heating assesses mantle heating. Using this simple subtraction suggests 4-6 TW of radiogenic mantle heating for the EH model, 9-12 TW for the CI model, and 18-28 TW for the GP model. Radiogenic heating and geo-neutrino production in the mantle vary significantly between geological models. Measuring the geo-neutrino flux from the mantle provides strong constraints on geological models.

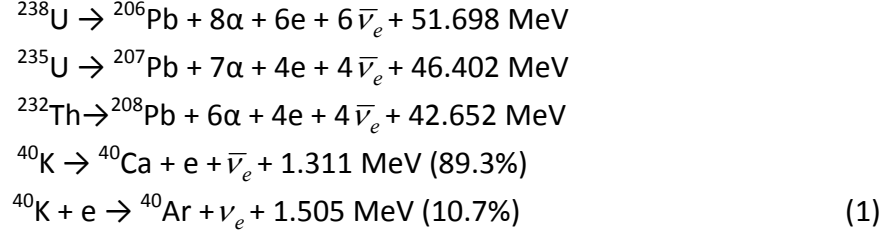
This Letter discusses the present status and future prospects of resolving geological models by geo-neutrino observations. It starts with the physics of geo-neutrinos, opening with an introduction to neutrinos (2) and proceeding with an evaluation of the antineutrino luminosity and radiogenic heating for uranium, thorium, and potassium (3). It completes the physics input with descriptions of geo-neutrino interactions, including the current detection technique (4) and the signal-distorting effects of neutrino oscillations (5). Shifting to geology, this Letter compares several model predictions for the quantity and distribution of terrestrial radiogenic heating (6). It continues with a discussion of the geological input needed to calculate the geo-neutrino signal (7). There follows a presentation and evaluation of recent geo-neutrino observations (8). This Letter closes by describing the capability of an oceanic geo-neutrino observatory for resolving earth models (9).

## **2. Neutrinos**

Neutrinos and antineutrinos have associations with three electrically charged leptons, namely the electron, mu, and tau. They are the lightest of the known massive particles and lack measureable electromagnetic properties (Giunti and Studenikin, 2009). Because their dominant interaction with other particles is the weak nuclear force, they transit vast amounts of matter without deflection or appreciable absorption. Neutrinos and antineutrinos, which are produced by nuclear processes inside stars and planets, carry off otherwise shrouded information about the interiors of these dense objects. Electron neutrinos emanate from the decay of neutron-poor nuclei, which are copiously produced by nuclear fusion inside stars. Electron antineutrinos emerge from the decay of neutron-rich nuclei, which are readily formed by nuclear fission reactors and naturally synthesized in supernovae. Detectable geo-neutrinos originate from terrestrial uranium and thorium, fused by an ancient stellar explosion, incorporated with the material forming the earth, and distributed by global differentiation.

### 3. Geo-neutrino production and energy spectra

Terrestrial isotopes of uranium, thorium, and potassium contribute significantly to the planetary energy budget (Van Schmus, 1995). These isotopes decay to stable nuclei with the release of energy and the emission geo-neutrinos according to:



Calculation of the decay energy ( $Q$ ) utilizes a standard table of atomic masses (Audi and Wapstra, 1995). The average amount of terrestrial heat per decay is the decay energy minus the average energy carried off by geo-neutrinos, which originate almost exclusively in beta decay.

$$[A, Z] \rightarrow [A, Z + 1] + e + \bar{\nu}_e + Q_\beta \tag{2}$$

Conservation laws define the energy and momentum of the emitted electron. Using energy units

$$w_e = (Q_\beta + m_e - E_{\bar{\nu}_e}) \text{ and } p_e = [(Q_\beta + m_e - E_{\bar{\nu}_e})^2 - m_e^2]^{1/2}. \tag{3}$$

To close approximation the energy spectrum of antineutrinos from beta decay is proportional to

$$dn(E_{\bar{\nu}_e})/dE_{\bar{\nu}_e} \propto w_e E_{\bar{\nu}_e}^2 p_e^{2\gamma-1} e^{\pi\eta} |\Gamma(\gamma + i\eta)|^2. \tag{4}$$

With  $\alpha$  the fine structure constant

$$\gamma = \sqrt{1 - \alpha^2(Z + 1)^2} \text{ and } \eta = \alpha(Z + 1)w_e/p_e. \tag{5}$$

Using the definitions in (3) gives the spectrum in terms of the antineutrino energy. The spectrum for each radioactive nuclide results from the sum of antineutrino spectra of all beta decays, leading to the stable daughter nucleus. These spectra contribute according to the branching ratios, fractional intensities, and endpoint energies of transitions to the various daughter nuclear states.

Figure 1 displays the antineutrino energy spectra per decay  $dn(E_{\bar{\nu}_e})/dE_{\bar{\nu}_e}$  for  ${}^{238}\text{U}$ ,  ${}^{235}\text{U}$ ,  ${}^{232}\text{Th}$ , and  ${}^{40}\text{K}$ . The area under each spectrum equals the number of emitted

antineutrinos per decay  $n_{\bar{\nu}_e}$  of each parent nuclide. Multiplying this number by the average energy of each spectrum estimates the energy escaping the earth on average per decay of each of the radioactive nuclides. The average energy of  $^{40}\text{K}$  requires a small correction, accounting for the emission of the neutrino from electron capture. Subtracting the average escape energy from the decay energy computes the radiogenic heat absorbed by the earth on average per decay ( $Q_h = Q - Q_\nu$ ). The calculated rate of heating per unit mass of the parent nuclide, or the isotopic heat generation, is

$$h = \frac{N_A \lambda}{\mu} Q_h, \quad (6)$$

with  $N_A$  Avogadro's number,  $\lambda$  the decay constant, and  $\mu$  the molar mass. Table 1 presents the quantities used to calculate the radiogenic power of  $^{238}\text{U}$ ,  $^{235}\text{U}$ ,  $^{232}\text{Th}$ , and  $^{40}\text{K}$ . These quantities also allow calculation of the isotopic antineutrino luminosity

$$l = \frac{N_A \lambda}{\mu} n_{\bar{\nu}_e}. \quad (7)$$

Element specific heat generation and antineutrino luminosity follow from summing the isotopic values weighted by natural abundance. Table 2 presents values for uranium, thorium and potassium. These agree with values from similar calculations (Enomoto et al., 2007; Fiorentini et al., 2007). Heat production values differ at the 4% level from estimates approximating the antineutrino energy (Rybach, 1988).

#### 4. Geo-neutrino detection

Geo-neutrino detection exploits a coincidence of signals from quasi-elastic scattering on a proton, following the traditional method for measuring reactor antineutrinos (Reines and Cowan, 1953). In this neutron inverse beta decay reaction, an electron antineutrino becomes a positron by collecting the electric charge from a proton, which becomes a neutron (Vogel and Beacom, 1999).



In organic scintillating liquid, the reaction products produce signals correlated in position and time. The positron retains most of the available energy, which is approximately the electron antineutrino energy ( $E_{\bar{\nu}_e}$ ) minus the difference in mass energy between the neutron and proton ( $\Delta = M_n - M_p$ ). It rapidly (<1 ns) loses kinetic energy through ionization of the scintillating liquid, producing a prompt signal proportional to the energy of the electron antineutrino.

$$T_e = E_{\bar{\nu}_e} - \Delta - m_e \quad (9)$$

The positron soon annihilates with an electron, releasing  $\gamma$ -rays with total energy equal to twice the electron mass. If the  $\gamma$ -rays interact within the scintillating liquid, typically by Compton scattering, this increases the energy and spatial spread of the prompt signal. Prior to annihilation, the positron has a significant probability ( $\sim 50\%$ ) of temporarily forming a bound state with an electron, delaying the annihilation signal by several nanoseconds (Franco et al., 2011). Although this delay degrades the positron position resolution, it helps reject background.

The neutron maintains most of the momentum of the electron antineutrino, initially moving forward and losing energy through collisions with hydrogen nuclei. Some of the recoiling protons contribute relatively small amounts of ionization energy to the prompt signal. After coming to thermal equilibrium, the neutron diffuses through the medium, typically for many microseconds before getting absorbed by an atomic nucleus within a meter of the original interaction. Adding a neutron to the atomic nucleus triggers a release of radiation from the newly-formed nuclide. Although reactor antineutrino experiments sometimes use gadolinium for neutron absorption, which decreases the diffusion time and significantly boosts the delayed signal (Bemporad et al., 2002), geo-neutrino observations detect the mono-energetic gamma ray from the formation of deuterium.



This delayed signal completes the temporal and spatial coincidence, confirming the detection of an electron antineutrino.

Detecting neutron inverse beta decay is an established method for measuring the energy spectrum of geo-neutrino interactions. The threshold energy is approximately the difference in mass energy between the neutron plus positron and the proton ( $\Delta + m_e \approx 1.8 \text{ MeV}$ ). There is no sensitivity to geo-neutrinos with energy below this threshold, masking completely the contributions of  $^{235}\text{U}$  and  $^{40}\text{K}$ . Above the threshold energy the cross section grows approximately as the square of the antineutrino energy minus the neutron-proton mass energy difference (Vogel and Beacom, 1999).

$$\sigma_p(E_{\bar{\nu}_e}) = 9.52(E_{\bar{\nu}_e} - \Delta)^2 \sqrt{1 - m_e^2 / (E_{\bar{\nu}_e} - \Delta)^2} \times 10^{-44} \text{ cm}^2 \quad (11)$$

A less developed method of detecting electron antineutrinos involves elastic scattering on atomic electrons (Reines et al., 1976).



There is no energy threshold for this process, giving sensitivity to geo-neutrinos with energy below the neutron inverse beta decay threshold. The signal, however, is simply

the recoiling electron. The lack of a coincidence tag and an intense flux of solar neutrinos make exploiting this reaction challenging. However, the electrons scatter in the forward direction, suggesting signal sensitivity through resolution of the electron direction. The maximum kinetic energy of the electrons is

$$T_{\max} = \frac{E_{\bar{\nu}_e}}{1 + m_e/2E_{\bar{\nu}_e}}. \quad (13)$$

With the dependence on the weak mixing angle given by  $x = 2\sin^2\theta_W$ , the cross section is

$$\sigma_e(E_{\bar{\nu}_e}) = 0.43 \left[ x^2 T_{\max} + (x+1)^2 \frac{E_{\bar{\nu}_e}}{3} \left\{ 1 - \left( 1 - \frac{T_{\max}}{E_{\bar{\nu}_e}} \right)^3 \right\} - x(x+1) \frac{m_e T_{\max}^2}{2E_{\bar{\nu}_e}^2} \right] \times 10^{-44} \text{ cm}^2. \quad (14)$$

The cross section for electron neutrino elastic scattering on electrons, which lacks interference between neutral and charged currents, is larger by a factor of 2.36. This exacerbates the background from solar neutrinos.

Figure 2 displays the electron antineutrino cross sections over the range of energy relevant for geo-neutrino studies both for quasi-elastic scattering on protons and elastic scattering on electrons. Although electron scattering provides sensitivity to geo-neutrinos from  $^{40}\text{K}$  and  $^{235}\text{U}$  and has an advantage of four electron targets for each proton in organic scintillating liquid, it requires further development. Therefore, geo-neutrino detection by electron scattering is not considered further in this Letter.

The product of the antineutrino energy spectra for  $^{238}\text{U}$ ,  $^{235}\text{U}$ ,  $^{232}\text{Th}$ , and  $^{40}\text{K}$  (Fig. 1) and the quasi-elastic proton scattering cross section gives the differential geo-neutrino signal spectra. Figure 3 displays the spectra of  $^{238}\text{U}$  and  $^{232}\text{Th}$  interactions per decay per proton. The number of antineutrinos per decay of the parent nuclide divided by the area under each curve calculates the flux of geo-neutrinos required to produce one interaction. The magnitude of this flux commands the exposure of geo-neutrino observations. It is convenient to scale this flux to one interaction during a fully efficient one-year exposure of  $10^{32}$  protons, called a terrestrial neutrino unit (TNU) (Mantovani et al., 2004). This scaling provides the signal-to-flux conversion factors

$$C_U = 7.6 \times 10^4 \text{ cm}^{-2} \text{ s}^{-1} \text{ TNU}^{-1} \text{ and } C_{Th} = 2.5 \times 10^5 \text{ cm}^{-2} \text{ s}^{-1} \text{ TNU}^{-1}. \quad (15)$$

These factors, which agree with the results of previous calculations (Enomoto et al., 2007; Fiorentini et al., 2007), are sensitive to the shape of the beta decay spectrum (Fiorentini et al., 2010).

## 5. Geo-neutrino propagation

Detectable geo-neutrinos travel at or near the speed of light in the vacuum (Longo, 1987), providing an instantaneous view of terrestrial radioactivity. Neutrino oscillation diminishes the detectable geo-neutrino signal below inverse-square scaling, depending on energy and distance (Araki et al., 2005a). The survival probability of electron antineutrinos for three-neutrino mixing is

$$P_{ee}^{3\nu} = 1 - \{ \cos^4(\theta_{13}) \sin^2(2\theta_{12}) \sin^2(\Delta_{21}) + \sin^2(2\theta_{13}) [\cos^2(2\theta_{12}) \sin^2(\Delta_{31}) + \sin^2(2\theta_{12}) \sin^2(\Delta_{32})] \}, \quad (16)$$

where  $\theta_{12}$  and  $\theta_{13}$  are mixing angles,  $\Delta_{ji} = 1.27(|\delta m_{ji}^2|L)/E_{\bar{\nu}_e}$  control the oscillations with  $\delta m_{ji}^2 \equiv m_j^2 - m_i^2$  the neutrino mass-squared difference of  $\nu_j$  and  $\nu_i$  in  $\text{eV}^2$ ,  $L$  is the neutrino flight distance in meters, and  $E_{\bar{\nu}_e}$  is the antineutrino energy in MeV. Experimental evidence limits the subdominant mixing angle  $\theta_{13}$  to a small though possibly non-zero value (Fogli et al., 2011). This suggests simplifying the survival probability to the two-neutrino mixing form

$$P_{ee} \cong 1 - \sin^2(2\theta_{12}) \sin^2(\Delta_{21}). \quad (17)$$

A 2 MeV geo-neutrino has an oscillation length of 65 +/-2 km, which is about 1% of the radius of the earth. These determinations prompt an approximate expression for the average geo-neutrino survival probability, specifically

$$\langle P_{ee} \rangle \cong 1 - 0.5 \sin^2(2\theta_{12}). \quad (18)$$

Using the value of  $\theta_{12}$  from a global, three-neutrino analysis (Fogli et al., 2011) sets the average survival probability at .575 +/- .012. Uncertainty in the average survival probability of a few percent is small in comparison with the precision of present experimental results.

## 6. Quantity and distribution of terrestrial radioactivity

Previous sections present the physics input required for calculating radiogenic heating and surface geo-neutrino signal. Geological models guide the remaining input, specifying the quantity and distribution of uranium, thorium, and potassium. This section reviews geological model predictions.

Three compositionally distinct, concentric shells comprise the earth. These terrestrial volumes, called the core, mantle, and crust, are the result of primordial planet differentiation. In the standard scenario, the planet grows by the accretion of condensates from the solar nebula. These planetesimals, containing trace amounts of uranium and thorium and minor amounts of potassium, are representative of primitive,

undifferentiated chondritic meteorites (Wasson and Kallemeyn, 1988). The falling planetesimals heat the proto earth, forming silicate and metallic melts. Density differentiates a metallic core sunk beneath a silicate mantle, on top of which floats a silicate crust. Seismology resolves the stratified shell-structure of the planet, identifying a solid inner and a liquid outer core, a lower and an upper mantle, and a lower, middle, and upper crust (Dziewonski and Anderson, 1981). Although seismology determines density and discriminates solid from fluid, it does not constrain the abundances of trace and minor elements. Chemical affinity, however, confines lithophilic uranium, thorium, and potassium to the silicate shell of the earth.

Although geochemistry predicts no radioactivity in the core (McDonough, 2003), geophysics entertains the possibility in order to reconcile the persistence and energy requirements of the geomagnetic field with the present size and growth rate of the solid inner core (Buffett, 2003; Davies, 2007). Laboratory measurements of the partitioning of elements between metal and silicates restrict the abundance of uranium in the core to <0.63 ppb (Malavergne, et al., 2007) and permit an abundance of potassium in the range of 60 -130 ppm, depending on sulfur content (Murthy, et al., 2003). At the upper limits of abundances uranium and potassium provide together ~1 TW of radiogenic heating in the core. Because this is a relatively insignificant amount on the global scale, the following assumes negligible radioactivity in the core.

Chemical earth models differ as to which group of chondritic meteorites represents the parent material of the earth. This leads to a discrepancy between the predicted amounts of terrestrial radiogenic heating even though both favored groups, the carbonaceous CI and the enstatite EH, have similar abundances of uranium and thorium. Moreover, this similarity manifests as a chondritic thorium to uranium mass ratio of ~3.9. In both the EH and CI earth models, formation of the metallic core increases the abundances of the heat-producing elements remaining in the silicate shell by a factor of ~1.5. The disparity in the radiogenic heating predictions results from differences in volatile element abundances. Whereas the CI group is rich in volatile elements, the EH group is highly depleted (Wasson and Kallemeyn, 1988). Because volatile elements can escape the accretion process, it can take more CI material than EH material to match the present mass of the earth. This effectively enriches refractory uranium and thorium abundances in a CI earth relative to an EH earth. Assuming ~40% CI mass loss due to non-condensation during accretion leads to an enrichment factor of 2.5, including core formation. Accordingly, the abundances of uranium and thorium in the silicate earth are higher than in the chondrites. The EH model with enrichment of 1.5 predicts  $12.6 \pm 1.4$  TW of terrestrial radiogenic heating, or 0.24-0.30 of the surface heat flow. The CI model with enrichment of 2.5 predicts  $18.4 \pm 1.1$  TW of terrestrial radiogenic heating, or 0.37-0.42 of the surface heat flow.

Physical earth models recognize mantle convection as the main mechanism for the transport of interior heat to the surface. Sufficient convection requires enough radiogenic heating within the mantle to influence the temperature-dependent mantle

viscosity. Convection calculations favoring a layered mantle predict  $30.7 \pm 3.8$  TW of terrestrial radiogenic heating (Turcotte et al., 2001), or 0.57-0.73 of the surface heat flow. Table 3 summarizes the relevant earth model information.

The chemical composition of the crust, including estimates of the abundances of uranium, thorium, and potassium in the upper, middle, and lower layers, is reasonably well-established (Rudnick and Gao, 2003). Seismology defines the thicknesses and densities of crust layers on a 2-degree by 2-degree grid (Bassin et al., 2001). Together these assess the masses of uranium, thorium, and potassium in the crust, estimating radiogenic heating at  $8.1 \pm 0.8$  TW. Table 4 summarizes the relevant crust model information.

The geo-dynamically important mantle comprises roughly two-thirds of the mass of the planet. Solid-state convection of the mantle is the dominant mechanism transporting heat to the surface. Internal radiogenic heating influences convection by regulating mantle viscosity. An assessment of radiogenic heating in the mantle is fundamental to understanding the thermal evolution of the planet.

Following the assumption of a non-radioactive core, makes the masses of uranium, thorium, and potassium in the mantle complementary to those in the crust. The amounts in the mantle and crust account for the full inventory in the planet. Subtracting the estimated crust amounts from the predicted amounts from the various earth models assesses the amounts in the mantle. This mass-balancing of elements predicts mantle radiogenic heating of  $4.6 \pm 1.6$  TW for the EH model,  $10.4 \pm 1.4$  TW for the CI model, and  $22.6 \pm 3.9$  TW for the GP model. Radiogenic heating in the mantle clearly differentiates these earth models. The corresponding geo-neutrino signal rates from the mantle reflect the predicted spread in mantle heating. These are  $4.2 \pm 1.5$  TNU for the EH model,  $8.9 \pm 1.6$  TNU for the CI model, and  $19.4 \pm 3.4$  TNU for the GP model. Variation in the above rates suggests measurements of the mantle geo-neutrino rate require precision of  $\pm 2$  TNU in order to resolve these earth models. Table 5 summarizes the relevant information for the derived mantle models.

A lower limit to the radiogenic heating in the mantle applies the composition of the depleted mantle, which forms mid-ocean ridge basalts. Two assessments, which agree within uncertainties, offer  $4.1 \pm 1.2$  TW (Salters and Stracke, 2004) and  $2.8 \pm 0.3$  TW (Workman and Hart, 2005). This amount of mantle heating is consistent with the prediction of the EH model, in disagreement with the predictions of the CI model, and significantly at odds with the prediction of the GP model. The depleted mantle composition assessments are useful for estimating the effects of a layer enriched in uranium and thorium at the base of the mantle, as suggested by measured differences in neodymium isotopic ratios in chondrites and terrestrial rocks (Boyet and Carlson, 2005). Table 6 presents relevant information for the depleted mantle assessments.

## 7. Terrestrial antineutrino signal

Model estimates of the quantity and distribution of radioactive isotopes within the earth allow calculation of the resulting geo-neutrino signal spectrum. The expression is

$$\frac{dN(E_{\bar{\nu}_e})}{dE_{\bar{\nu}_e}} = \varepsilon \frac{N_A \lambda}{\mu} \sigma_p(E_{\bar{\nu}_e}) \frac{dn(E_{\bar{\nu}_e})}{dE_{\bar{\nu}_e}} \langle P_{ee} \rangle \int_{\oplus} dV \frac{a(\bar{r}') \rho(\bar{r}')}{4\pi |\bar{r} - \bar{r}'|^2}, \quad (19)$$

where  $\varepsilon$  is the effective exposure of a detector at position  $\bar{r}$ ,  $a(\bar{r}')$  is the parent nuclide abundance distribution, and  $\rho(\bar{r}')$  is the earth density distribution. In principle, the effective exposure involves an energy-dependent efficiency for detecting geo-neutrino interactions. The geo-neutrino signal spectrum sums the contributions from the parent nuclides  $^{238}\text{U}$  and  $^{232}\text{Th}$ . If the abundance of a parent nuclide is uniform throughout a spherical shell, then the integral

$$G = \int_{shell} dV \frac{\rho(\bar{r}')}{4\pi |\bar{r} - \bar{r}'|^2} \quad (20)$$

calculates geological response factors (Krauss et al., 1984). Table 7 presents factors for the mantle and several sub-shells.

A prediction of the geo-neutrino signal rate in TNU from a geological reservoir  $G$  with uniform abundance of a parent nuclide is

$$R = C\varphi = Cl \langle P_{ee} \rangle Ga. \quad (21)$$

A prediction of the elemental radiogenic heating in watts due to a geo-neutrino flux  $\varphi$  from a geological reservoir  $G$  with mass  $M$  is

$$H = \frac{\varphi}{\langle P_{ee} \rangle} \frac{h M}{l G}. \quad (22)$$

If the mass ratio of thorium to uranium ( $\kappa = a_{Th}/a_U$ ) is uniform throughout the reservoir, then

$$\varphi_{Th}/\varphi_U = 0.217\kappa \text{ and } R_{Th}/R_U = 0.066\kappa. \quad (23)$$

These relationships are useful for interpreting existing geo-neutrino observations.

Given a measured geo-neutrino signal, application of the average neutrino survival probability overestimates the abundances of parent nuclides and underestimates the thorium-to-uranium ratio. Figure 4 shows the rising shift in the ratio of  $P_{ee}$  to  $\langle P_{ee} \rangle$  with energy for simulated continental and oceanic observations. The shift is more

pronounced at continental sites than at oceanic sites due to proximity to higher levels of uranium and thorium. Although these effects at the level of several percent are small in comparison with present experimental uncertainties, they warrant consideration in future measurements, especially at continental locations.

## 8. Geo-neutrino observations

Geo-neutrino observatories are in operation at two northern hemisphere locations, producing measurements of the signal rate. These measurements carry precision of about 40%. The following presents a uniform analysis to these results, leading to estimates of the radiogenic heat production and comparisons with the selected earth models.

### 8.1. KamLAND

The KamLAND collaboration reports an observation of  $841 \pm 29$  candidate antineutrino events during a  $3.49 \times 10^{32}$  p-y exposure of a detector under Mt. Ikenoyama ( $36.42^\circ$  N,  $137.31^\circ$  E) in Japan (Gando et al., 2011). They estimate  $730 \pm 32$  background events, primarily from nearby nuclear reactors. This leads to a background-subtracted geo-neutrino signal of  $111 +45/-43$  events, which excludes the null hypothesis at the 99.5% confidence level. Note that uncertainty in the predicted background ( $\pm 32$ ) is greater than the statistical error on the total number of observed events ( $\pm 29$ ), indicating that systematic uncertainty now dominates the precision of the KamLAND geo-neutrino signal. After correcting for detection efficiency, the background-subtracted geo-neutrino signal rate is  $40.0 \pm 10.5$  (stat)  $\pm 11.5$  (sys) TNU.

An unconstrained maximum likelihood analysis of the KamLAND data prefers 65 events from uranium and 33 events from thorium (Gando et al., 2011). Using the conversion factors in eq. (15) this corresponds to a flux (signal rate) of  $1.75 \text{ cm}^{-2}\mu\text{s}^{-1}$  (23.1 TNU) from uranium and  $3.15 \text{ cm}^{-2}\mu\text{s}^{-1}$  (12.6 TNU) from thorium. By eq. (23) this division of events implies a signal-averaged thorium-to-uranium mass ratio of 8.2, which is roughly twice the chondritic ratio. However, the one standard deviation uncertainty contour allows no events from either uranium or thorium. Deriving geological conclusions from the KamLAND data requires assumptions about the distribution of uranium and thorium in the source regions.

Assuming the KamLAND data result from a signal-averaged thorium-to-uranium mass ratio of 3.9 estimates  $4.3 +1.2/-1.1 \text{ cm}^{-2}\mu\text{s}^{-1}$  of flux or a signal rate of  $38 +11/-10$  TNU (Gando et al., 2011). This chondritic mass ratio specifies  $2.3 \pm 0.6 \text{ cm}^{-2}\mu\text{s}^{-1}$  of flux ( $30 \pm 8$  TNU) from uranium and  $2.0 +0.6/-0.5 \text{ cm}^{-2}\mu\text{s}^{-1}$  of flux ( $8 \pm 2$  TNU) from thorium. A detailed study of the crust, including variations in the local geology, predicts  $1.72 \pm 0.29 \text{ cm}^{-2}\mu\text{s}^{-1}$  of flux ( $22.6 \pm 3.8$  TNU) from uranium and  $1.45 \pm 0.25 \text{ cm}^{-2}\mu\text{s}^{-1}$  of flux ( $5.8 \pm 1.0$  TNU) from thorium (Enomoto et al., 2007). Guidance from another study assigns the 16% uncertainty (Coltorti et al., 2011). Assuming no contribution from the core finds  $1.2 \pm 1.3 \text{ cm}^{-2}\mu\text{s}^{-1}$  of mantle flux or a signal rate of  $10 \pm 11$  TNU.

The following presents the radiogenic heating values resulting from two possible distributions of uranium and thorium in the mantle, which are consistent with the mantle flux observed by KamLAND. A homogeneous distribution of uranium and thorium sets a lower limit of  $12 \pm 13$  TW of radiogenic heating in the mantle. An upper limit results from an enriched layer of heat-producing elements at the base of depleted homogeneous mantle (Salters and Stracke, 2004). This distribution leads to  $15 +18/-17$  TW of radiogenic heating in the mantle. Adding the crust contribution gives  $23 +18/-17$  TW and  $20 \pm 13$  TW of terrestrial radiogenic heating for a homogeneous mantle with and without an enriched basement layer, respectively. Comparing these results with the  $47 \pm 2$  TW surface heat flow concludes that the earth is cooling down (Gando et al., 2011).

## 8.2. Borexino

The Borexino collaboration reports an observation of 15 candidate antineutrino events from a  $0.179 \times 10^{32}$  p-y exposure of a detector under Mt. Aquila ( $42.45^\circ$  N,  $13.57^\circ$  E) in Italy (Bellini et al., 2010). They estimate  $5.0 \pm 0.3$  events from nearby nuclear reactors and  $0.31 \pm 0.05$  events from non-antineutrino sources. This leads to a background-subtracted geo-neutrino signal of  $9.7 \pm 3.9$  events, which excludes the null hypothesis at the 99.4% confidence level. Note that statistical error on the total number of observed events ( $\pm 3.9$ ) is much greater than the uncertainty in the predicted background ( $\pm 0.3$ ). The reported systematic error demonstrates the potential for measuring the geo-neutrino signal with an ultimate precision of less than 10%. This is due in part to the remarkable radio-purity of the Borexino detector. After correcting for detection efficiency, the background-subtracted geo-neutrino signal rate is  $64 \pm 25$  (stat)  $\pm 2$  (sys) TNU.

An unconstrained maximum-likelihood analysis of the Borexino data prefers  $9.9 +4.1/-3.4$  events (Bellini et al., 2010). As with the KamLAND data, the present precision of the Borexino data prevents geological conclusions without assumptions about the distribution of uranium and thorium in the source regions. Assuming the Borexino data result from a signal-averaged thorium-to-uranium mass ratio of 3.9 estimates  $7.3 +3.0/-2.5 \text{ cm}^{-2}\mu\text{s}^{-1}$  of flux or a signal rate of  $65 +27/-22$  TNU. This chondritic mass ratio specifies  $3.9 +1.6/-1.4 \text{ cm}^{-2}\mu\text{s}^{-1}$  of flux ( $51 +21/-18$  TNU) from uranium and  $3.3 +1.4/-1.1 \text{ cm}^{-2}\mu\text{s}^{-1}$  of flux ( $13 +6/-4$  TNU) from thorium. A detailed study of the crust, including variations in the local geology, predicts  $1.57 \pm 0.25 \text{ cm}^{-2}\mu\text{s}^{-1}$  of flux ( $20.7 \pm 3.3$  TNU) from uranium and  $1.43 \pm 0.22 \text{ cm}^{-2}\mu\text{s}^{-1}$  of flux ( $5.7 \pm 0.9$  TNU) from thorium (Coltorti et al., 2011). Assuming no contribution from the core finds  $4.3 +3.1/-2.5 \text{ cm}^{-2}\mu\text{s}^{-1}$  of mantle flux or a signal rate of  $39 +27/-23$  TNU.

The following presents the radiogenic heating values resulting from two possible distributions of uranium and thorium in the mantle, which are consistent with the mantle flux observed by Borexino. A homogeneous distribution of uranium and thorium sets a lower limit of  $45 +32/-26$  TW of radiogenic heating in the mantle. An upper limit results from an enriched layer of heat-producing elements at the base of depleted homogeneous mantle (Salters and Stracke, 2004). This distribution leads to  $58 +42/-35$

TW of radiogenic heating in the mantle. Adding the crust contribution gives  $66 +42/-35$  TW and  $53 +32/-26$  TW of terrestrial radiogenic heating for a homogeneous mantle with and without an enriched basement layer, respectively. These results do not constrain the thermal evolution of the earth.

## 9. Discussion

Independent observations of the surface geo-neutrino signal by two detectors separated by about  $120^\circ$  of longitude in the northern hemisphere now exist. Each observation has a precision slightly under 40%. Geological conclusions assume the observations exhibit the chondritic thorium-to-uranium mass ratio. Figure 5 compares the KamLAND and Borexino geo-neutrino observations with the selected model predictions. Whereas the KamLAND result is consistent with each of the earth models selected for comparison herein, the Borexino result is consistent with only the geophysical model (GP) and in mild disagreement with the geochemical models (EH and CI). Neither assessment carries precision sufficient for resolving these models. The KamLAND measurement is limited by systematic uncertainty of the background and the Borexino measurement is limited by low statistics. Combining these observations with detailed predictions of the crust signal allows assessments of the mantle signal, no contribution from the metallic core. Even though the mantle signal observed by Borexino ( $39 +27/-23$  TNU) is consistent with the KamLAND result ( $10 \pm 11$  TNU), it is tempting to speculate that this higher value is due to proximity to the large low shear velocity province beneath the African continent (Garnero and McNamara, 2008). Applying several geology-based assumptions the KamLAND data allow global radiogenic heating of  $23 +18/-17$  TW, indicating the earth is cooling down. The corresponding result from Borexino data is  $66 +42/-35$  TW, which is inconclusive.

The apparent challenges confronting KamLAND and Borexino prompt an evaluation of the capability of future observatories for resolving earth models. Several new projects with sensitivity to the surface geo-neutrino signal are planning the deployment of detectors in the continental crust. These include SNO+ ( $46.47^\circ$  N,  $278.80^\circ$  E) near Sudbury, Canada (Chen 2006) and LENA ( $63.66^\circ$  N,  $26.05^\circ$  E) near Pyhäsalmi, Finland (Hochmuth et al., 2006). The precision of the geo-neutrino signal measurements from these future projects is likely to reach below 10%, which is a significant improvement over the present 40% level. However, without a corresponding reduction in the uncertainty of the crust signal prediction, measurements from these projects are unlikely to resolve earth models. Uncertainty of about 15% in the predicted crust signal rate ( $\sim 40$  TNU) at these continental locations saddles the assessed mantle rate with a systematic error of about 6 TNU. This error is comparable to the differences between the mantle signal rates predicted by the selected earth models. Moreover, model predictions of the thorium-to-uranium ratio of the signals observed at these continental locations have relatively small differences. Compounding the challenges of model discrimination at continental locations is the rate shift and spectral distortion introduced by using the average neutrino survival probability. This distortion is enhanced at locations with increased levels of uranium and thorium, such as the

Sudbury basin (Perry et al., 2009). Unless geological studies are capable of significantly improving knowledge of the uranium and thorium distribution within the crust, it is not possible to resolve the selected earth models through observations at continental sites.

Deploying a detector in the ocean basin far from continental crust and nuclear power reactors allows maximal sensitivity to the geo-neutrino signal from the mantle (Rothschild et al., 1998). The predicted signal from the crust at such a site is less than 4 TNU (Enomoto et al., 2007). Applying the typical crust rate uncertainty of about 15% suggests a systematic error of less than 1 TNU in the measured mantle signal rate, including uncertainty in the reactor background and number of proton targets (Dye 2010). Discriminating the signals predicted by the selected earth models at the oceanic site becomes a statistical issue of detector exposure. Constraining the end member models requires a relatively modest exposure of less than  $2 \times 10^{32}$  p-y. Error in the mantle-rate measurement remains dominated by statistics for exposures of 20–50  $\times 10^{32}$  p-y, depending on the model. A project to build and operate a movable deep ocean antineutrino observatory capable of such exposures is under development (Dye et al., 2006).

In addition to confirming previous assertions of the geological utility of measuring the mantle geo-neutrino rate at an oceanic location (Rothschild et al., 1998; Enomoto, et al., 2007; Gando et al., 2011; Mareschal et al., 2011), this Letter presents the advantage of measuring the geo-neutrino spectrum to assess the thorium-to-uranium ratio. This information helps constrain earth models. Figure 6 compares the selected model predictions for a typical continental site (Sudbury) and a typical oceanic site (Pacific). The oceanic site facilitates model discrimination by signal rate and thorium-to-uranium ratio. An observatory in Oceania could measure the geo-neutrino rate and spectrum with the precision required to resolve earth models and assess terrestrial radiogenic heating, thereby constraining the origin and thermal history of the planet.

### **Acknowledgements**

This work was supported in part by National Science Foundation grants (#0855838 and #1068097) and by the Hawaii Pacific University trustee scholarship fund.

### **References**

Araki, T., et al., 2005a. Measurement of neutrino oscillation with KamLAND: Evidence of spectral distortion. *Phys. Rev. Lett.* 94, 081801.

Araki, T., et al., 2005b. Experimental investigation of geologically produced antineutrinos with KamLAND. *Nature* 436, 499–503.

Arevalo, R. Jr., McDonough, W.F., Luong, M., 2009. The K/U ratio of the silicate Earth: Insights into mantle composition, structure and thermal evolution. *Earth Planet. Sci. Lett.* 278, 361-369.

Audi, G., Wapstra, A.H., 1995. The 1995 update to the atomic mass evaluation. Nucl. Phys. A 595, 409-480.

Bassin, C., Laske, G., Masters, G., 2000. The current limits of resolution for surface wave tomography in North America. EOS Trans. Am. Geophys. Union 81, F897 <http://igppweb.ucsd.edu/~gabi/crust2.html>.

Bellini, G., et al., 2010. Observation of geo-neutrinos. Phys. Lett. B 687, 299–304.

Bemporad, C., Gratta, G., Vogel, P., 2002. Reactor-based neutrino oscillation experiments. Rev. Mod. Phys. 74, 297-328.

Boyet, M., Carlson, R.W., 2005.  $^{142}\text{Nd}$  evidence for early (>4.53 Ga) global differentiation of the silicate earth. Science 309, 576–581.

Buffett, B.A., 2003. The thermal state of earth's core. Science 299, 1675-1677.

Chen, M.C., 2006. Geo-neutrinos in SNO+. Earth Moon Planet 99, 221-228.

Coltorti, M., et al., 2011. U and Th content in the Central Apennines continental crust: A contribution to the determination of the geo-neutrinos flux at LNGS. Geochim. Cosmochim. Acta 75, 2271-2294.

Davies, G.F., 2007. Mantle regulation of core cooling: A geodynamo without core radioactivity? Phys. Earth Planet. Interiors 160, 215-229.

Davies, J.H., Davies, D.R., 2010. Earth's surface heat flux. Solid Earth 1, 5-24.

Dye, S.T. et al., 2006. Earth radioactivity measurements with a deep ocean antineutrino observatory. Earth Moon Planet 99, 241-252.

Dye, S.T., 2010. Geo-neutrinos and silicate earth enrichment of U and Th. Earth Planet Sci. Lett. 297, 1-9.

Dziewonski, A.M., Anderson, D.L., 1981. Preliminary Reference Earth Model (PREM). Phys. Earth Planet. Inter. 25, 297–356.

Enomoto, S., et al., 2007. Neutrino geophysics with KamLAND and future prospects. Earth Planet. Sci. Lett. 258, 147-159.

Fiorentini, G. et al., 2005. How much uranium is in the earth? Predictions for geoneutrinos at KamLAND. Phys. Rev. D 72, 033017.

Fiorentini, G. et al., 2007. Geo-neutrinos and earth's interior. Phys. Rep. 453, 117-172.

Fiorentini, G. et al., 2010. Nuclear physics for geo-neutrino studies. *Phys. Rev. C* 81, 034602.

Fogli, G.L. et al., 2011. Evidence for  $\theta_{13}>0$  from global neutrino data analysis. *Phys. Rev. D* 84, 053007.

Franco, D., Consolati, G., Trezzi, D., 2011. Positronium signature in organic liquid scintillators for neutrino experiments. *Phys. Rev. C* 83, 015504.

Gando, A. et al., 2011. Partial radiogenic heat model for Earth revealed by geoneutrino measurements. *Nature Geosci.* DOI: 10.1038/NGEO1205.

Garnero, E.J., McNamara, A.K., 2008. Structure and dynamics of earth's lower mantle. *Science* 320, 626-628.

Giunti, C., Studenikin, A., 2009. Neutrino electromagnetic properties. *Phys. At. Nucl.* 72, 2089–2125.

Hochmuth, K.A. et al., 2006. Probing earth's interior with the LENA detector. *Earth Moon Planet* 99, 253-264.

Jaupart, C., Labrosse, S., Mareschal, J.-C., 2007. Temperature, heat and energy in the mantle of the earth. In: Schubert, G. (Ed.), *Treatise on Geophysics*, vol. 7. Elsevier, New York, pp. 253–303.

Javoy, M. et al., 2010. The chemical composition of the earth: enstatite chondrite models. *Earth Planet. Sci. Lett.* 293, 259-268.

Korenaga, J., 2008. Urey ratio and the structure and evolution of Earth's mantle. *Rev. Geophys.* 46, RG2007.

Krauss, L.M., Glashow, S.L., Schramm, D.N., 1984. Antineutrino astronomy and geophysics. *Nature* 310, 191-198.

Lay, T., Hernlund, J., Buffett, B.A., 2008. Core-mantle boundary heat flow. *Nature Geosci.* 1, 25-32.

Longo, M.J., 1987. Tests of relativity from SN1987A. *Phys. Rev. D* 36, 3276-3277.

Malavergne, V. et al., 2007. New high-pressure and high-temperature metal/silicate partitioning of U and Pb: Implications for the cores of the Earth and Mars. *Geochim. Cosmochim. Acta* 71, 2637-2655.

Mantovanti, F. et al., 2004. Antineutrinos from Earth: a reference model and its uncertainties. *Phys. Rev. D* 69, 013001.

Mareschal, J.-C. et al., 2011. Geoneutrinos and the energy budget of the earth. *J. Geodynam.* 54, 43-54.

McDonough, 2003. Compositional model for the earth's core. In: Carlson, R.W., Holland, H.D., Turekian, K.K. (Eds.), *Treatise on Geochemistry*, vol. 2. Elsevier, New York, pp. 547-568.

Murthy, V.R., van Westrenen, W., Fei, Y., 2003. Experimental evidence that potassium is a substantial radioactive heat source in planetary cores. *Nature* 423, 163-165.

Palme, H. and Jones, A., 2003. Solar system abundances of the elements. In: Holland, H.D., Turekian, K.K. (Eds.), *Treatise on Geochemistry*, vol. 1. Elsevier, Amsterdam, pp. 41-61.

Perry, H.K.C., Mareschal, J.-C., Jaupart, C., 2009. Enhanced crustal geo-neutrino production near the Sudbury Neutrino Observatory, Ontario, Canada. *Earth Planet. Sci. Lett.* 288, 301-308.

Reines, F. and Cowan Jr., C.L., 1953. Detection of the free neutrino. *Phys. Rev.* 92, 830-831.

Reines, F., Gurr, H.S., Sobel, H.W., 1976. Detection of  $\bar{\nu}_e - e$  scattering. *Phys. Rev. Lett.* 37, 315-318.

Rocholl, A., Jochum, K.P., 1993. Th, U and other trace elements in carbonaceous chondrites: Implications for the terrestrial and solar system Th/U ratios. *Earth Planet. Sci. Lett.* 117, 265-278.

Rothschild, C.G., Chen, M.C., Calaprice, F.P., 1998. Antineutrino geophysics with liquid scintillator detectors. *Geophys. Res. Lett.* 25, 1083-1086.

Rudnick, R.L., Gao, S., 2003. Composition of the continental crust. In: Holland, H., Turekian, K.K. (Eds.), *Treatise on Geochemistry*, vol. 3. Elsevier, New York, pp. 1-64.

Rybach, L., 1988. Determination of heat production rate. In: Haenel, R., Rybach, L., Stegena, L. (Eds.), *Handbook of Terrestrial Heat-flow Density Determinations*, Kluwer, Amsterdam, pp. 125-142.

Salters, V.J.M., Stracke, A., 2004. Composition of the depleted mantle. *Geochem. Geophys. Geosyst.* 5, Q05004.

Turcotte, D.L., Paul, D., White, W.M., 2001. Thorium-uranium systematics require layered mantle convection. *J. Geophys. Res.* 106, 4265-4276.

Van Schmus, W.R., 1995. Natural radioactivity of the crust and mantle. *Global Earth Physics: A Handbook of Physical Constants*. Am. Geophys. Union, Washington, DC, pp. 283–291.

Vogel, P., Beacom, J.F., 1999. Angular distribution of neutron inverse beta decay,  $\bar{\nu}_e + p \rightarrow e^+ + n$ . *Phys. Rev. D* 60, 053003.

Wasson, J.T., Kallemeyn, G.W., 1988. Compositions of Chondrites. *Philos. Trans. R. Soc. Lond. A* 325, 535-544.

Workman, R.K., Hart, S.R., 2005. Major and trace element composition of the depleted MORB mantle (DMM). *Earth Planet. Sci. Lett.* 231, 53–72.

Table 1. Relevant quantities for the parent nuclides principally responsible to radiogenic heating and geoneutrino flux.

Isotope	% n. a.	$\mu(\text{g/mol})$	$\lambda(10^{-18} \text{ s}^{-1})$	$n_{\bar{\nu}_e}$	$Q(\text{pJ})$	$Q_v(\text{pJ})$	$Q_h(\text{pJ})$	$h(\mu\text{W/kg})$	$l(\text{kg}^{-1}\mu\text{s}^{-1})$
$^{238}\text{U}$	99.2796	238	4.916	6	8.282	0.634	7.648	95.13	74.6
$^{235}\text{U}$	0.7204	235	31.210	4	7.434	0.325	7.108	568.47	319.9
$^{232}\text{Th}$	100.0000	232	1.563	4	6.833	0.358	6.475	26.28	16.2
$^{40}\text{K}$	0.0117	40	17.200	0.893	0.213	0.116	0.110	28.47	231.2

Table 2. Element specific heat generation and antineutrino luminosity per unit mass.

	$h(\mu\text{W/kg})$	$l(\text{kg}^{-1}\mu\text{s}^{-1})$
Uranium	98.5	76.4
Thorium	26.3	16.2
Potassium	$3.33 \times 10^{-3}$	$27.1 \times 10^{-3}$

Table 3. Silicate earth model information. Potassium abundances from K/U=13,800±1300 (Arevalo et al., 2009).

Silicate earth ( $M_{SE} = 4.03 \times 10^{24} \text{ kg}$ )	$a_U(\text{ng/g})$	$a_{Th}(\text{ng/g})$	Th/U	$a_K(\mu\text{g/g})$	$P_h(\text{TW})$
Chem-EH (J et 2010)	14 (±10%)	45 (±10%)	3.3	190 (±14%)	12.6±1.4
Chem-CI (RJ 93)	19 (±8%)	72 (±5%)	3.9	260 (±12%)	18.4±1.1
Phys-GP (TPW 01)	30 (±12%)	120 (±12%)	4.0	420 (±15%)	30.7±3.8

Table 4. Crust model information.

Crust ( $M_C = 27.9 \times 10^{21} \text{ kg}$ )	$M(10^{21} \text{ kg})$	$a_U(10^{-6} \text{ g/g})$	$a_{Th}(10^{-6} \text{ g/g})$	Th/U	$a_K(10^{-2} \text{ g/g})$	$P_h(\text{TW})$
CC sediments	0.8	2.7 (±21%)	10.5 (±10%)	3.9	2.4 (±8%)	0.5 ± 0.1
CC Upper	6.9	2.7 (±21%)	10.5 (±10%)	3.9	2.4 (±8%)	4.3 ± 0.6
CC Middle	7.1	1.3 (±31%)	6.5 (±8%)	5.0	2.0 (±14%)	2.6 ± 0.4
CC Lower	6.5	0.2 (±80%)	1.2 (±80%)	6.0	0.5 (±30%)	0.4 ± 0.3
OC sediments	0.3	1.7 (±20%)	6.9 (±10%)	4.1	1.5 (±10%)	0.1 ± 0.0
OC	6.3	0.1 (±20%)	0.2 (±10%)	2.2	0.1 (±10%)	0.1 ± 0.0
Bulk Crust	27.9	1.2 (±15%)	5.0 (±7%)	4.3	1.3 (±7%)	8.1 ± 0.8

Table 5. Derived homogeneous mantle model information.

Mantle ( $M_M = 4.00 \times 10^{24} \text{ kg}$ )	$a_U(\text{ng/g})$	$a_{Th}(\text{ng/g})$	Th/U	$a_K(\mu\text{g/g})$	R (TNU)	$P_h(\text{TW})$
Chem-EH (J et 2010)	5.5 (±34%)	11 (±49%)	1.9	95 (±28%)	4.2±1.5	4.6±1.6
Chem-CI (RJ 93)	11 (±19%)	38 (±12%)	3.6	165 (±20%)	8.9±1.6	10.4±1.4
Phys-GP (TPW 01)	23 (±18%)	88 (±17%)	3.8	330 (±16%)	19.4±3.4	22.6±3.9

Table 6. Depleted mantle model information (mantle minus D'').

Depleted Mantle ( $M_{DM} = 3.87 \times 10^{24} \text{ kg}$ )	$a_U(\text{ng/g})$	$a_{Th}(\text{ng/g})$	Th/U	$a_K(\mu\text{g/g})$	$P_h(\text{TW})$
Salters & Stracke 2004	4.7 (±30%)	14 (±30%)	2.9	65 (±31%)	4.1±1.2
Workman & Hart 2005	3.2 (±14%)	7.9 (±14%)	2.5	44 (±17%)	2.8±0.3

Table 7. Geological response factors and masses of deep earth reservoirs.

	In. Core	Out. Core	Core	D''	Low. Mantle	Up. Mantle	Mantle
$G(10^5 \text{ kg cm}^{-2})$	0.19	3.86	4.06	0.29	7.32	4.16	11.77
$M(10^{24} \text{ kg})$	0.10	1.84	1.94	0.13	2.81	1.06	4.00

## Figure Captions

Fig. 1. These curves show the antineutrino spectra for the main nuclides contributing to terrestrial radiogenic heating and the surface geo-neutrino flux.

Fig. 2. These curves show the total cross sections for the scattering of electron antineutrinos on protons and electrons over the range of energy relevant to geo-neutrinos. For reference the cross section for electron neutrino scattering on electrons is also shown, being about a factor of 2.36 larger than that for electron antineutrinos.

Fig. 3. These curves show the interaction spectra per proton target for antineutrinos from  $^{238}\text{U}$  and  $^{232}\text{Th}$ .

Fig. 4. An upward shift and distortion of the energy spectrum is introduced by using the average oscillation probability. The shift and distortion are more pronounced at a continental site than at an oceanic site. Simulations consider a continental planet with 45-km thick crust and an oceanic planet with 8-km thick crust. The continental observatory is 2-km below the surface, while the oceanic observatory is 0.1-km above the crust.

Fig. 5. This figure compares the KamLAND (left panel) and Borexino (right panel) measurements with the selected model predictions.

Fig. 6. This figure compares the predicted signals at the Sudbury site (left panel) and the Pacific site (right panel). Differences in the model signals are pronounced in both rate and spectrum at the Pacific site.

Figure 1

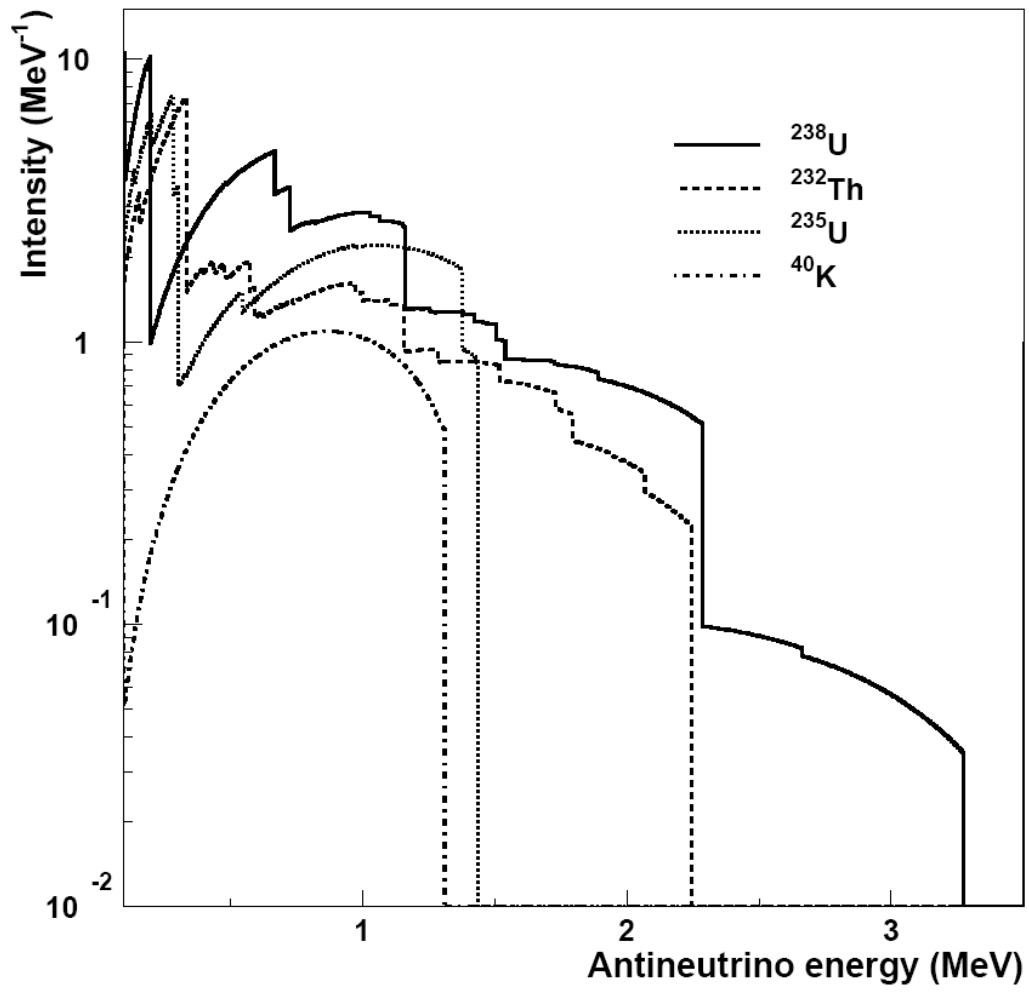


Figure 2

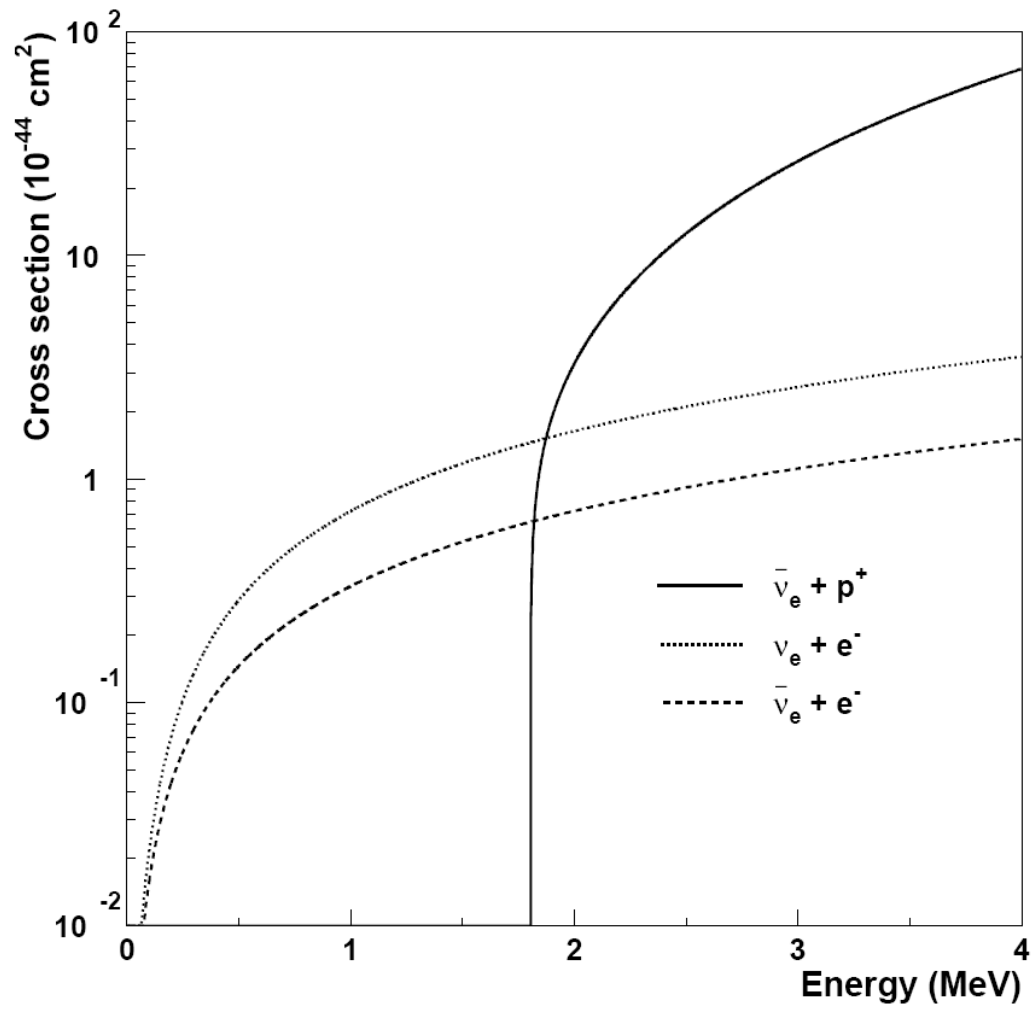


Figure 3

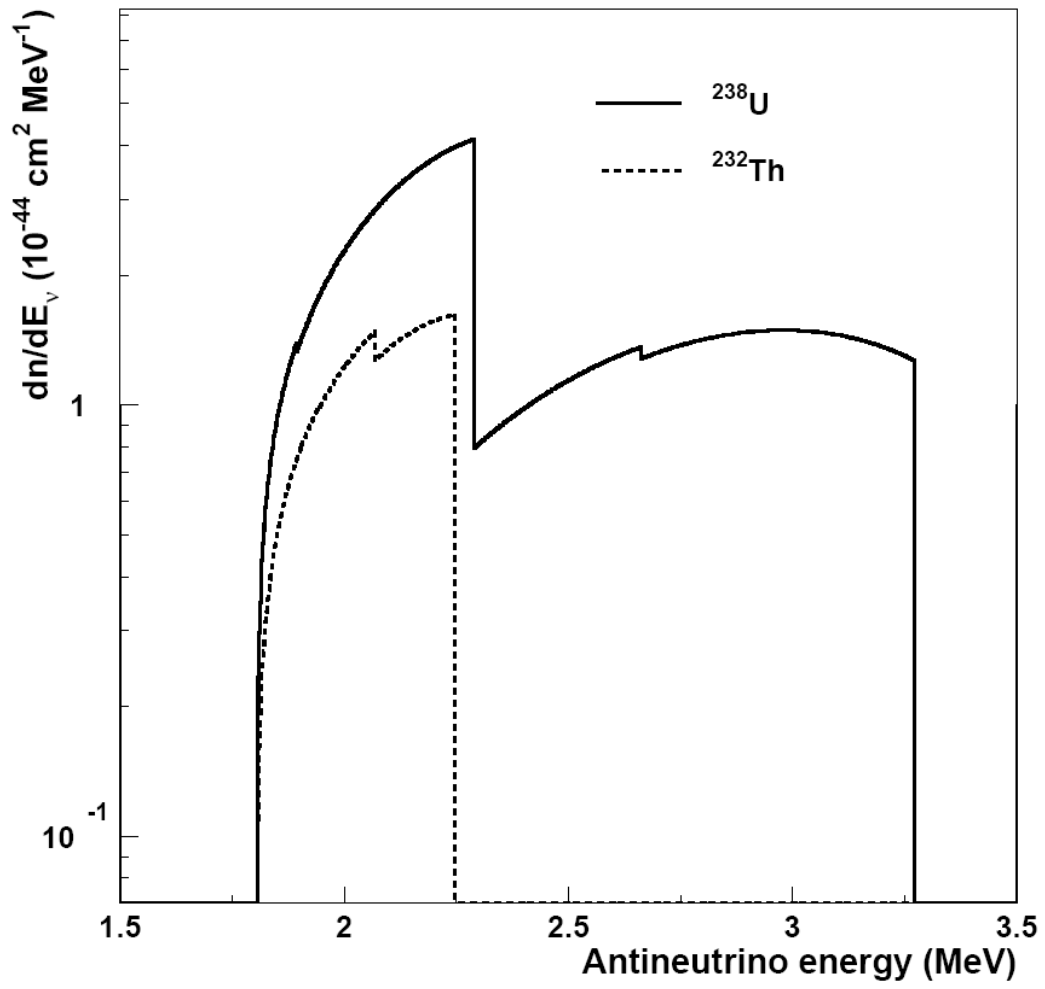


Figure 4

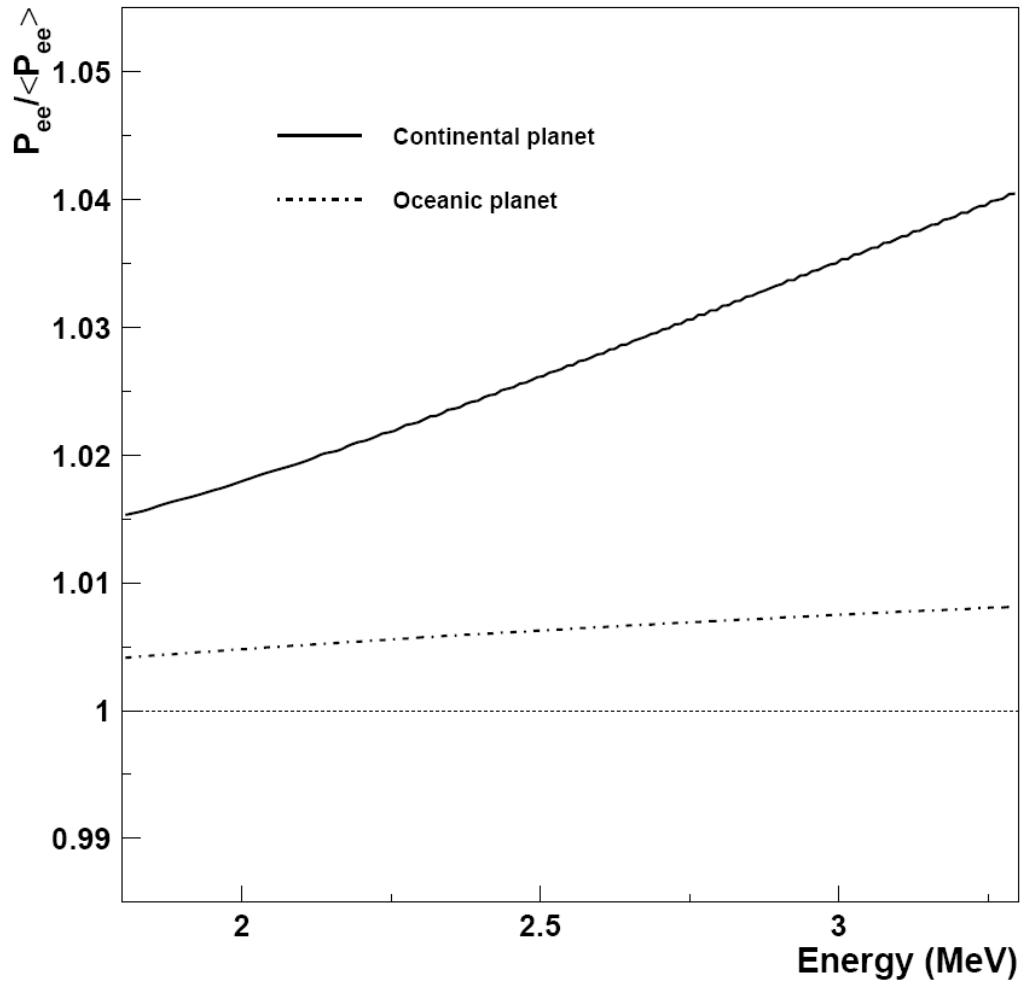


Figure 5

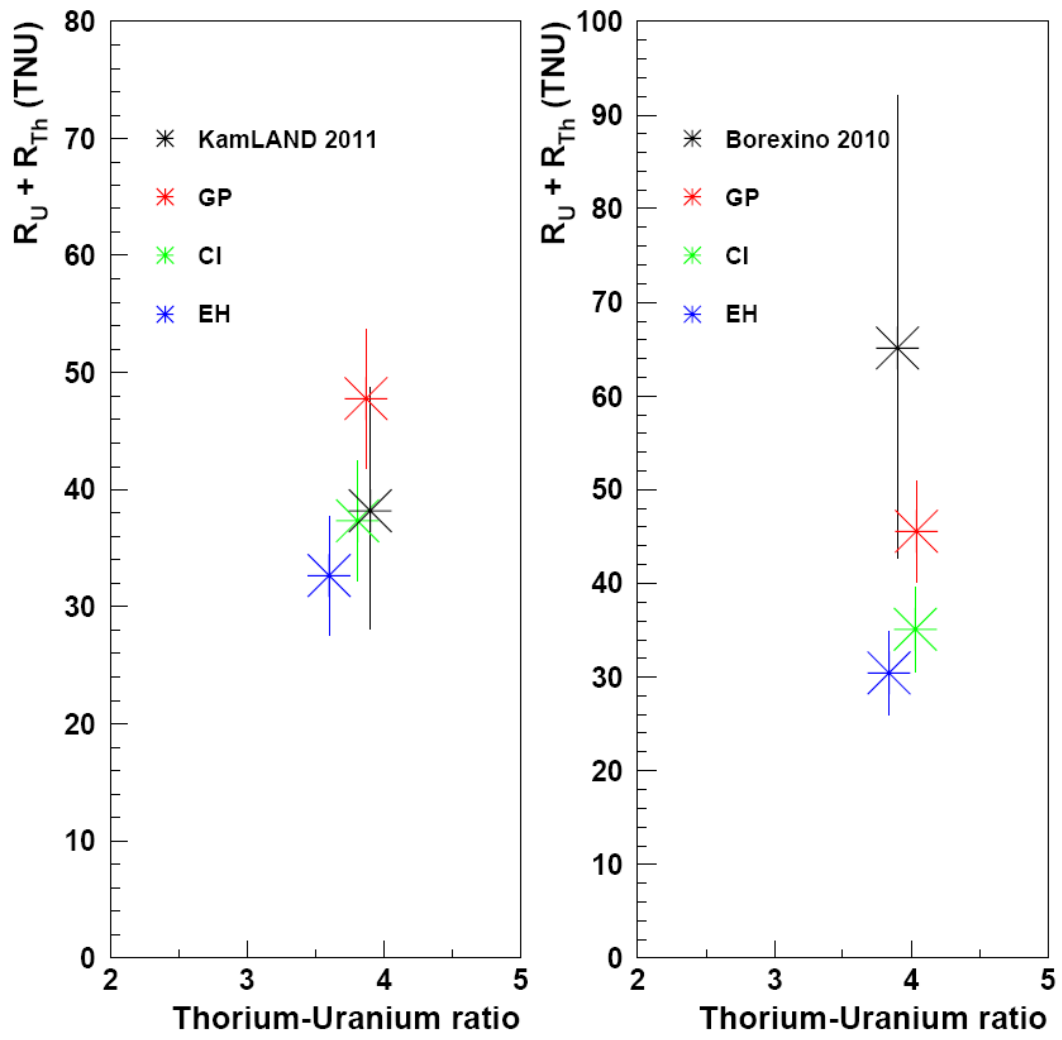


Figure 6

